Volume 1 | Number 1 | Jan 2013 | Pages 1–100

Journal of
Materials Chemistry A

Materials for energy and sustainability
www.rsc.org/materialsA

ROYAL SOCIETY OF CHEMISTRY

www.rsc.org/materialsA

Journal of Materials Chemistry A

ARTICLE

N-doped carbon encapsulated ultrathin MoO₃ nanosheets as superior anode with high capacity and excellent rate capability for Li-ion batteries

Jiyicheng Qiu[a], Zhanxu Yang[a*], Yue Li[b]

Molybdenum oxide is an attractive anode material of lithium ion batteries because of its environmental benignity and high capacity. However, molybdenum oxide suffers from serious capacity fading caused by large volume change and poor rate capability due to low conductivity. In this work, ultrathin N-doped carbon layer encapsulated MoO₃ nanosheets have been synthesized by a simultaneous pyrolysis-reduction process of dodecylamine-intercalated MoO₃ composites at 600 °C under nitrogen atmosphere. This special 2D nanosheet morphology can greatly shorten the diffusion length of both electrons and ions, which can ensure fast kinetics of Li⁺ intercalation and deintercalation, resulting in high rate performance. Furthermore, N-doped carbon encapsulated MoO₃ nanosheets exhibited good electrical conductivity, uniform dispersion and ultrathin thickness. On the basis of these combined effects, the as-fabricated nanosheets can reach high initial charge and discharge capacity of 1610 and 1359 mAh g⁻¹, and show remarkable cycle stability with a specific capacity of 1250 mAh g⁻¹ after 60 cycles at 0.3 C rate. High specific discharge capacities are maintained at fast C rates, e.g., 1370, 1010, 940, 610, 490 and 370 mAh g⁻¹ at 0.3 C, 1 C, 2 C, 4 C, 10 C, and 20 C, respectively.

1 Introduction

As an attractive anode material for lithium ion batteries (LIBs), molybdenum oxide(e.g., MoO_2[1,2] and MoO_3[3-7]) has been the focus in recent years due to its high theoretical capacity, low cost, and environmental friendly nature. Nevertheless, the low electrical conductivity of pristine molybdenum oxide challenges the achievement of high capacity at high current rates.[8,9] On the other hand, electrical contact between active materials and current collector/conductive carbon is easily destroyed due to drastic volume change caused by the conversion reaction of oxide materials during the charge/discharge process, leading to a continual capacity loss and poor rate properties.[10-12] The nanostructural electrode materials could significantly relieve the structural strains without pulverization upon lithiation and delithiation, which can help electrode materials obtain good rate performance.[13] However, high specific surface area of nanosized materials also increases excessive Li⁺ consumption from side reactions of electrode and electrolyte, producing large irreversible capacity loss and poor cycling life.[14,15] Furthermore, the aggregation of nanograins during cycling

process remains unsolved. The incorporation of carbonaceous materials, e.g., carbon layers onto metal oxides at the nanoscale, proves to be effective in enhancing the conductivity of the composites and preventing the direct contact of active materials with the electrolytes.[16-18] In addition, the good buffering effect and mechanical strength can benefit electrode materials to achieve an enhanced cycling performance and rate capability.[19-22]

Recently two dimensional (2D) nanosheets have aroused increasing interest due to their intrinsic physical and chemical features.[23,24] 2D nanosheet can not only shorten the lithium ion transportation path, but also guarantee the facile strain relaxation and reduce the fracture that occurs inside bulk materials. In particular, it was reported that such unique 2D morphology can significantly promote the host capability of active electrode materials.[25-27] Meanwhile, many researches have shown that N-doping is an effective way to improve the electrochemical performance of carbon materials.[28] Nitrogen doping offers high electronic conductivity and more active sites for Li⁺ insertion/extraction in the N-doped carbon, which further brings great advancement in reversible capacity and rate capability of active materials.[29-33] Therefore, inspired by unique properties of 2D nanosheet morphology and N-doped carbon-coating advantage, we here present a novel strategy to synthesize MoO₃ nanosheets encapsulated with N-doped carbon (NC) layer, designated as MoO₃/NC nanosheets. The fabrication process of the nanosheets involves a simultaneous pyrolysis-reduction process, in which MoO₃/NC nanosheet is prepared from layered MoO₃/dodecylamine precursor via the decomposition of dodecylamine as nitrogen source between

College of Chemistry, Chemical Engineering and Environment Engineering, Liaoning Shihua University, Fushun, Liaoning 113001, P. R. China

E-mail: zhanxuy@126.com

School of Foreign Languages, Liaoning Shihua University, Fushun, Liaoning 113001, P. R. China.

This journal is © The Royal Society of Chemistry 20xx

J. Mater. Chem. A, 20xx, 00, 1-3 | 1

ARTICLE

1 layers. In this way, thin nitrogen-doped carbon layer can be
2 produced and a little amount of MoC can be formed on the
3 surface of MoO_3, both of which are beneficial for improving
4 molybdenum oxide conductivity. The good structural flexibility
5 and mechanical strength of nitrogen-doped carbon can keep
6 the structural stability of hybrid.[34-37] Importantly, 2D
7 nanosheet-type structure can be well retained through in-situ
8 simultaneous pyrolysis-reduction of the intercalation structure,
9 which would offer combined effects of structural attachment
10 and chemical coupling between MoO_3 and N-doped carbon
11 more fully than ex-situ hybridization to buffer drastic volume
12 change during the cycling process and preserve electric
13 connection, thus leading to excellent cycling stability.
14 With this design, the following advantages are summarized
15 from the MoO_3/NC anode materials: (1) the as-obtained
16 nanoarchitecture is the 2D nanosheets-like structure derived
17 from layered MoO_3/dodecylamine precursor, which can greatly
18 facilitate the transportation of Li^+ and electron, while the high
19 surface area allows for a large contact area of electrode with
20 the electrolyte, thus providing good kinetics of lithium and
21 electrons diffusion; (2) nitrogen-doping can not only improve
22 the conductivity of the composites, but also create more
23 defects and active site for lithium storage and the enhancement
24 of rate capability. Meanwhile, carbon component decreases the
25 electrochemically active area exposed to electrolyte, which
26 increases cycle life; (3) nitrogen-doped carbon layer can
27 diminish mechanical pulverization efficiently and maintain the
28 structural integrity upon Li^+ insertion/extraction, thus
29 minimizing detachment between active materials and current
30 collector/conductive carbon and reducing the irreversible
31 capacity loss. Therefore, the MoO_3/NC nanosheets show
32 remarkable rate capability and high reversible capacity.

33 ## Experimental

34 ### Material preparation

35 5 mL dodecylamine and 58 mL anhydrous ethanol were mixed
36 and stirred for 10 min. Subsequently, 0.57 g α-MoO_3 was added
37 to the above solution and the mixture was heated to 70 ^{o}C for
38 24 h. Having been filtered, washed with anhydrous ethanol and
39 dried at 60 ^{o}C for 24 h in a vacuum oven, white power samples
40 obtained were precursor composite. The as-prepared precursor
41 was heated to various temperatures (200, 300, 400, 500, 600,
42 700, and 800 ^{o}C) and was held for 2 h under flowing N_2
43 protection to prepare final products. These samples were
44 designed as M-200, M-300, M-400, M-500, M-600, M-700, and
45 M-800, respectively.

46 ### Material characterization

47 X-ray powder diffraction (XRD) measurements were obtained
48 on Bruker D8 Advance diffractometer operated at 40 kV and 40
49 mA in the range 1.5-70 ° with Cu-K$_\alpha$ radiation (λ=0.15406 nm).
50 The particle morphologies of the products were observed by
51 means of a field emission scanning electron microscope (FE-
52 SEM) (Hitachi SU 8010) operated at an acceleration voltage of
53 15 kV. High-resolution transmission electron microscope
54 (HRTEM) was performed on a JEM-2100 microscope (JEOL). In-

55 situ Fourier Translation-Infrared Spectroscopy (in-situ FT-IR)
56 was recorded on Nicolet 380 spectrometer (Thermo Fisher
57 Scientific). Thermogravimetric-Mass Spectrometry (TG-MS)
58 combination was performed with STA 449 F5 (NETZSCH) up to
59 700 ^{o}C under argon flow with a heating rate of 10 ^{o}C min^{-1}. X-
60 ray photoelectron spectroscopic (XPS) measurement of the
61 composites was conducted on ESCALAB 250 spectroscopy
62 (Thermo Fisher Scientific) with an Al K$_\alpha$ (1486.6 eV) X-ray source
63 operated at 15 kV and 150 mW. Element analysis performed on
64 CE-440 elemental analyzer (Exeter Analytical, Inc) was
65 employed to measure carbonaceous composition in various
66 samples at combustion temperature 980 ^{o}C and reduction
67 temperature 700 ^{o}C in a mixture of He and O_2 gas. Raman
68 spectra were recorded on the DXR Raman microscope (Thermo
69 Scientific) with a 532 nm excitation laser (setting 3 mW power,
70 10 s exposure time, 20 accumulations).

71 ### Electrochemical measurements

72 The working electrodes were made by coating a paste of active
73 materials, Super P, and binder (polyvinylidene fluoride, PVDF) in
74 a weight ratio of 80:10:10 on a copper-foil collector.
75 The active mass loading of about 0.8 mg cm^{-2} was employed in
76 this work. The electrode film was subjected to roll press and
77 electrodes of 10 mm diameter were punched out. The negative
78 electrodes were dried at 110 °C for 12 h in a vacuum oven.
79 Coin-type cells (CR 2032) were assembled in an argon filled
80 glove box with an electrolyte of 1 mol L^{-1} LiPF$_6$ in EC-EMC-DMC
81 (1:1:1 volume ratio) solution and a separator of Celgard 2400.
82 The electrochemical data were collected using LAND CT2001A
83 test system within the potential range of 0.01-3.0 V (vs. Li/Li$^+$).
84 The assembly of the cell was conducted in an Ar-filled glove-box
85 followed by an overnight aging treatment before the test.
86 Cycling voltammetry (CV) was measured at a scan rate of 0.5
87 mV s^{-1} using a CHI 660C electrochemical workstation (Shanghai
88 CHI Instruments). Electrochemical impedance spectroscopy (EIS)
89 was performed in the frequency range of 0.01-10^5 Hz on the
90 PARSTAT 2273 electrochemical workstation (Ametek).

91 ## Results and discussion

92 The fabrication process of M-600 nanosheets is schematically
93 shown in Fig. 1a. The morphology of M-600 nanosheets was
94 first examined by SEM and TEM characterizations. It can be
95 seen that the resulting samples exhibited 2D nanosheet-shaped
96 morphology with size of several micrometers (Fig. 1b,c).
97 Furthermore, the HRTEM image of M-600 validated the
98 presence of thin MoO_3 nanosheets and thin N-doped carbon
99 layer. The thickness of MoO_3 nanosheet is evaluated to be 10
100 nm, and the interspace of the layers is around 0.69 nm (bottom
101 inset in Fig. 1c). Interestingly, the surface of the MoO_3
102 nanosheet was uniformly covered with a thin nitrogen doped
103 carbon layer derived from the direct pyrolysis of dodecylamine
104 intercalated into layered MoO_3 layer. As illustrated in Fig. 1d,

2 | *J. Mater. Chem. A*, 20xx, **00**, 1-3

This journal is © The Royal Society of Chemistry 20xx
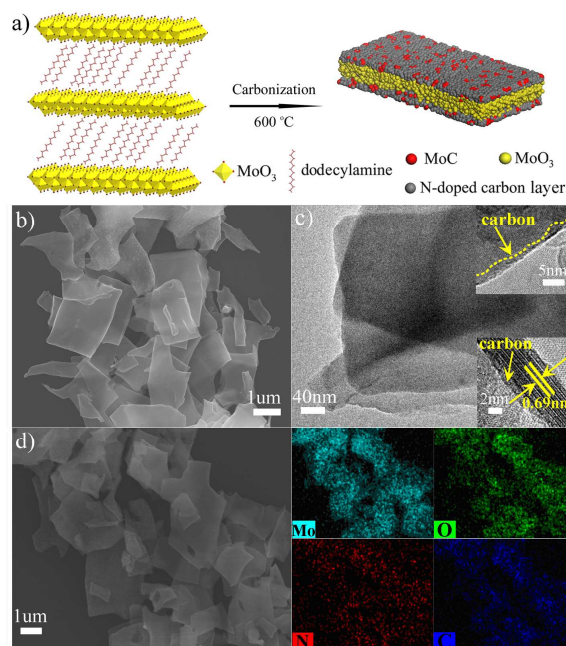
Fig. 1 (a)Schematic of the fabrication process of MoO₃/NC nanosheets. (b) SEM image of surface of sample M-600. (c) The TEM image of M-600. The insets of Fig. 1c show the HRTEM image of M-600. HRTEM show the presence of thin MoO₃ nanosheets and thin N-doped carbon layer. (d) The Element mapping of M-600.

the element mapping characterizations demonstrated that the nanosheets were composed of evenly molybdenum, oxygen, carbon and nitrogen. In addition, the local area magnification of elemental mapping from M-600 sample (Fig. S2) can further validate the distributed uniformity of carbon layer on MoO₃ nanosheets. HRTEM in Fig. S1h showed well-defined lattice fringes with a spacing of 0.25 nm corresponding to the (111) plane of MoC. The typical SEM images of α-MoO₃ and precursor MoO₃/dodecylamine were presented in Fig. S1a,b. Compared with bulk MoO₃ and precursor, M-600 is much thinner. Additionally, the morphology of M-700 due to varied composition was distinctly different from that of M-600, which might be associated with severe agglomeration of nanoparticles at high temperature in Fig. S1c.

According to the XRD pattern in Fig. S3a, the (010) diffraction peak of precursor with the strongest intensity at about 2.86 ^{o} corresponds to the interlayer gallery of 3.08 nm, which indicates that dodecylamine has been introduced to the interlayer between MoO₃ layers according to the previous literature.[38] From Fig. 2, it can be found that the (010) diffraction of intercalated composites moved to high angle with calcination temperature increasing from 200 to 500 ^{o}C, which revealed that the interlamellar spacing gradually shortened due to the decomposition of intercalated dodecylamine. In spite of interlayer shrinking due to dodecylamine decomposition, the existence of (010) diffraction revealed that remaining carbon materials still stayed in the interspace. Further increasing temperature to 600 ^{o}C, the (010) reflection completely
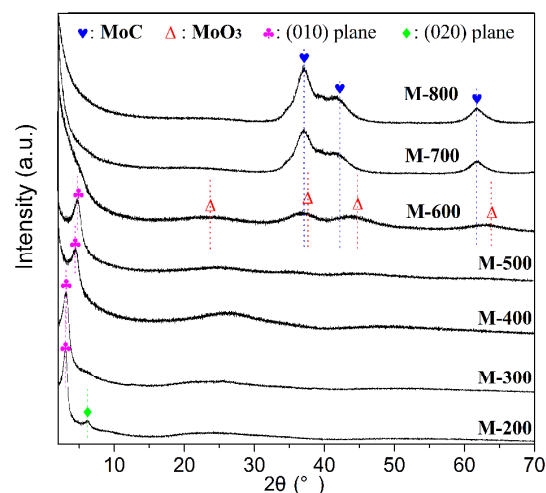
Fig. 2 XRD pattern of different composites after heating treatment at various temperatures.

disappeared, which implied that intercalated structure collapsed. Despite the broad and weak peaks here, the diffraction pattern of M-600 was well indexed to MoO₃ (mp-715463, IUCr), and MoC (JCPDS no.89-2868) also existed in M-600. As for M-700 and M-800, only diffraction peaks corresponding to MoC were identified, and the intensity increases. The SEM images of bare M-200, M-300, M-400 and M-500 were illustrated in Fig. S1d-g. It was apparent that the surface of both M-200 and M-300 were sags and crests. In contrast to M-200 and M-300, M-400 and M-500 demonstrated more smooth surfaces. Moreover, it was found that the thickness of corresponding samples gradually decreased with calcination temperature increasing and the sizes of calcined samples were smaller than that of precursor MoO₃/dodecylamine or MoO₃ (Fig. S1a,b). Simultaneously, M-500 presented similar nanosheets-type morphology with M-600.

To get insight into the formation mechanism underlying the generation of nanosheet-structural MoO₃/N-doped carbon hybrids, In-situ IR and TG-MS combination were used to investigate the in-situ evolution of the precursor during carbonization reaction. *In-situ* IR spectrum (Fig. S3b) showed that the intensity of absorption band from 2800 to 3000 cm^{-1}, corresponding to C-H stretching vibrations, gradually decreased with the increasing annealing temperature, which also provided evidence for dodecylamine decomposition. The reduced intensity suggested that long carbon chain of dodecylamine was carbonized. In particular, TG-MS combination (Fig. S3c) was used to analyze the pyrolysis of precursor MoO₃/dodecylamine in calcination process. It was clear that large weight loss of samples proceeded in the temperature range of 200~500 ^{o}C, which indicated that large amount of matter was lost from interlayers. Mass Spectrometry also detected high concentration of gas molecules (mainly including primary amine, C_nH_{2n+1}, C_nH_{2n} and their chemical rearrangement products) emission during calcination from 200 to 500 ^{o}C.

On the basis of above results, it is reasonable to presume that the formation of nanosheet-structural MoO₃/N-doped

This journal is © The Royal Society of Chemistry 20xx

J. Mater. Chem. A, 2015, **00**, 1-3 | **3**

1 carbon hybrids go through gas volume expansion process
2 accompanied with carbothermal reduction. When temperature
3 increases from 200 to 500 ^{o}C, dodecylamine breaks down into
4 massive gas molecules. The escape of gas molecules from
5 interlayers causes interlamellar spacing shrinkage and reduces
6 thickness of samples. In the gas emission process, the gas
7 would drastically expand when it is heated. The volume
8 expansion causes molybdenum oxide layers to burst and peel
9 off, which further etches the thickness of composites and leads
10 to surface roughness. With temperature rising up to 600 ^{o}C, the
11 carbonization effect of carbonaceous molecules and enormous
12 loss of gas molecules make layered structure collapse into
13 sheet-like structure. In addition, residue carbonaceous matters
14 form the carbon layer coating on the surface of molybdenum
15 oxide. As temperature rises, complete carbonizing degree of
16 residue carbon materials makes the surface of samples
17 gradually flat. At 600 ^{o}C, in-situ carburization of molybdenum
18 oxides by carbon materials produces small amount of MoC.

19   The contents of carbonaceous matters in various composites
20 were measured by elemental analyzer. The weight percentages
21 of carbon materials in M-500, M-600 and M-700 were 25.7%,
22 29.2% and 28.8%, respectively. Thus the contents of
23 molybdenum compounds in M-500, M-600 and M-700 were
24 calculated to be 74.3%, 70.8% and 71.2%, respectively.

25   Fig. 3a represented the XPS analysis of M-600, in which the
26 signals of Mo3d and N1s were observed, respectively. The
27 Mo3d spectra showed six peaks, which corresponded to $3d_{5/2}$
28 (228.8 eV) and $3d_{3/2}$ (231.7 eV) of Mo-C, $3d_{5/2}$ (230 eV) and $3d_{3/2}$
29 (233 eV) of Mo^{4+}, as well as $3d_{5/2}$ (232.3 eV) and $3d_{3/2}$ (235.4 eV)
30 of Mo^{6+}. Mo^{4+} was derived from the partial reduction of Mo^{6+}
31 occurring in the carbonization process. The peak at 398.4 eV in
32 N1s spectra was attributed to pyridinic-N, which can
33 significantly enhance the electrochemical activation of graphitic
34 carbon. Meanwhile, relative studies reports that the strong
35 interaction Mo-N (397.3 eV) can also improve the conductivity
36 of molybdenum oxide.[39-44] Fig. 3b showed the XPS for M-600
37 after etching 10 nm. It was clear that the Mo3d spectra exhibits
38 only three oxide state (Mo^{4+}, Mo^{5+} and Mo^{6+}) and has no Mo-C
39 bond, which reveals that the MoC phase just emerges on the
40 surface of M-600 composites. The XPS analyses for M-500 and
41 M-700 were presented in Fig. S4a and Fig. S4b for comparison.
42 The N1s spectra for M-500 contained pyrrolic-N (400.1 eV)
43 besides pyridinic-N. For M-700, the peak at 399.8 eV
44 corresponds to pyridonic-N.[45] By calculating the relative peak
45 fitting area of respective N configuration to the total peak area
46 in High-resolution N1s spectra,[46-54] it was further revealed that
47 M-600 contained more pyridinic-N (36.5%) than M-500 (32.6%)
48 and M-700 (23.3%). Among various N-dopant types, pyridinic-N
49 carbon is more favorable for lithium storage.[55-63] Therefore, M-
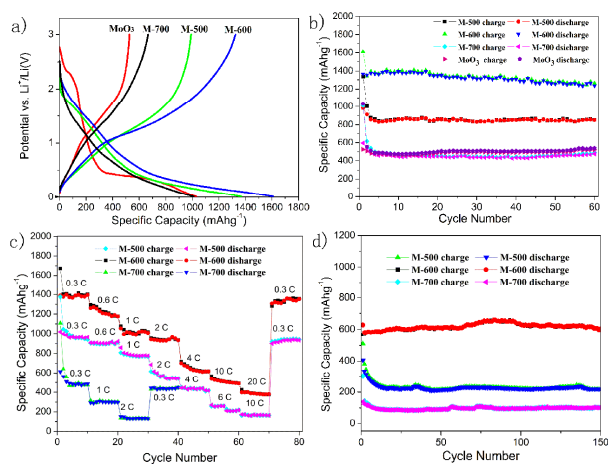50 600 has better reaction activity than M-500 and M-700.

51   Raman spectroscopy gives a more favored characterization of
52 the graphitization of carbon species. From Fig. S5a, D mode of
53 Raman spectra for corresponding products gradually became
54 discernible and G band shifted to higher frequency with
55 temperature rising from 200 to 400 ^{o}C, which implied that the
56 degree of graphitization increased as the temperature rose.
57 Each of Raman spectra for M-400, M-500, M-600, and M-700
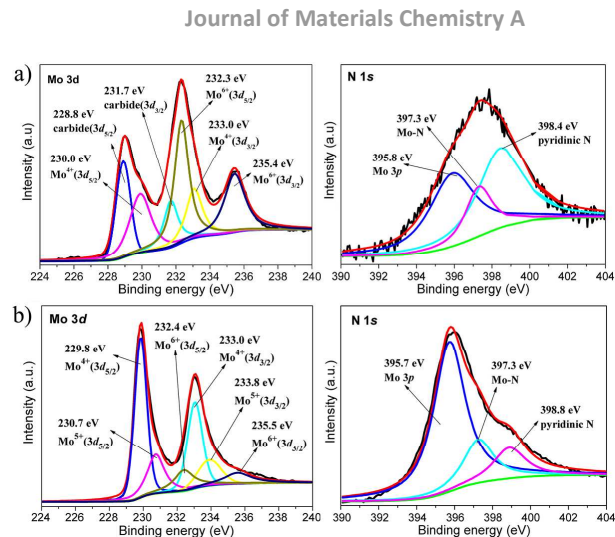
58
59 **Fig. 3** (a) XPS spectra of M-600 for Mo3d and N1s. (b) XPS
60 spectra of M-600 for Mo3d and N1s after etching 10 nm.

61
62
63 displayed remarkable D and G band around 1360 cm^{-1} and 1590
64 cm^{-1}. The relative peak integrated intensity ratio of the D/G
65 bands (I_D/I_G) is to judge the degree of graphitization. As shown
66 in Fig. S5b-e, the I_D/I_G of M-400, M-500, M-600, and M-700
67 were 0.69, 0.81, 1.01 and 1.39, respectively. In addition, the
68 FWHM of the G band for M-400, M-500, M-600 and M-700
69 were listed in Table S1 as follows. The FWHM of G bands for
70 these samples were all more than 50 cm^{-1}. It is accepted that if
71 the FWHM of the G band is larger than 50 cm^{-1}, the graphitic
72 cluster sizes in amorphous carbon are generally smaller than 1
73 nm.[64,65] Ferrari et al.[66] points out that, for small clusters (< 2 nm)
74 of aromatic rings in carbon, the D bands intensity increases
75 with the clusters growing, that is, the intensity ratio I_D/I_G rises
76 with the graphitic domain size increasing. Hence, it is certain
77 that M-700 and M-600 can reach higher graphitization degree
78 than M-400 and M-500. However, taking into account the fact
79 that the formation of molybdenum carbide depletes graphitic
80 carbon in M-700, M-600 should have more graphitic carbon
81 than M-700.

82   The electrochemical lithium storage properties of α-MoO$_3$,
83 M-500, M-700 and M-600 were evaluated by galvanostatic
84 charge/discharge voltage profiles at 0.3 C in a voltage windows
85 of 0.01-3.0 V, as shown in Fig. 4a. In particular, the total mass of
86 composite electrode was used to calculate the specific capacity.
87 The initial charge capacities of 1610 mAh g^{-1} with the initial
88 discharge capacities of 1359 mAh g^{-1} can be delivered in M-600,
89 which were higher than that of α-MoO$_3$ (1029 and 529 mAh g^{-1}),
90 M-500 (1364 and 991 mAh g^{-1}) and M-700 (1010 and 667 mAh
91 g^{-1}). The irreversible capacity loss of first cycle may be ascribed
92 to the formation of solid electrolyte interface on the surface of
93 electrode. Furthermore, the hysteresis (ΔEp) of the charge and
94 discharge plateaus for M-600 were obviously lower than that
95 for other three samples, which indicated that M-600 possessed
96 a more favorable kinetic for fast Li$^+$ insertion/extraction. Fig. 4b
97 showed the cyclability of MoO$_3$, M-500, M-600 and M-700. The
98 high reversible capacities of 1250 mAh g^{-1} were still delivered
99 for M-600 after 60 cycles at 0.3 C, higher than that of α-MoO$_3$

4 | *J. Mater. Chem. A*, 20xx, **00**, 1-3

This journal is © The Royal Society of Chemistry 20xx

1
2 **Fig. 4** (a) The charge/discharge voltage of MoO_3, M-500, M-600
3 and M-700 at the first cycle between 0.01-3.0 V (vs Li^+/Li) with a
4 current rate 0.3 C. (b) Cyclability tests on MoO_3, M-500, M-600
5 and M-700 at a current density of 0.3 C. (c) The rate
6 performance of M-500, M-600 and M-700 at different current
7 rate from 0.3~20 C. (d) Cyclability tests on M-500 at 6 C, M-600
8 at 6 C and M-700 at 4 C.
9
10
11 (520 mAh g^{-1}), M-500 (850 mAh g^{-1}) and M-700 (490 mAh g^{-1}).
12 The reversible capacities for M-600 were three times more than
13 the capacities of 372 mAh g^{-1} obtained for graphite anodes. To
14 investigate the rate performance of M-500, M-600 and M-700
15 composite electrode, the cell was cycled at various rates. As
16 shown in Fig. 4c, M-600 gave higher reversible capacities than
17 those of M-500 and M-700 at various rates. The reversible
18 capacities obtained were 1370, 1010, 940, 610, 490 and 370
19 mAh g^{-1} for 0.3 C (0.41 A g^{-1}), 1 C (0.93 A g^{-1}), 2 C (1.8 A g^{-1}), 4 C
20 (3.3 A g^{-1}), 10 C (6.2 A g^{-1})and 20 C (8.3 A g^{-1}). When the current
21 rate was brought down to 0.3 C after cycling at 20 C, the
22 capacity of the anode gradually recovered to 1350 mAh g^{-1},
23 which suggested that the structure of M-600 remained
24 exceedingly stable even under a high rate. The microstructures
25 of M-600 materials and pristine MoO_3 materials after 60 cycles
26 of charge-discharge at 1C were examined by SEM
27 characterization. As shown in Fig. S6, the morphology of
28 pristine MoO_3 after cycling has destroyed and pristine MoO_3
29 has been broken into very small pieces. But 2D sheet-like
30 morphology of M-600 materials was still retained, which
31 reveals that N-doped carbon coating on the surface of MoO_3
32 nanosheets can act as a barrier to reduce the aggregation and
33 thus increase the structural strength of M-600 composites
34 during cycling. Fig. 4d showed the cyclability test of 150 cycles
35 on M-500, M-600 and M-700 electrodes at high current rate.
36 After 150 cycles, M-600 remained the capacities of 605 mAh g^{-1}
37 at 6 C, which was higher than that values of M-500 (219 mAh g^{-1}
38 at 6 C) and M-700 (101 mAh g^{-1} at 4 C). The results demonstrate
39 that M-600 have good cycle stability. The electrochemical
40 performance of M-600 were also compared with that of pristine
41 α-MoO_3 nanosheets. Mostly recent study showed that pristine
42 α-MoO_3 nanosheets exhibited reversible capacities of 1110,
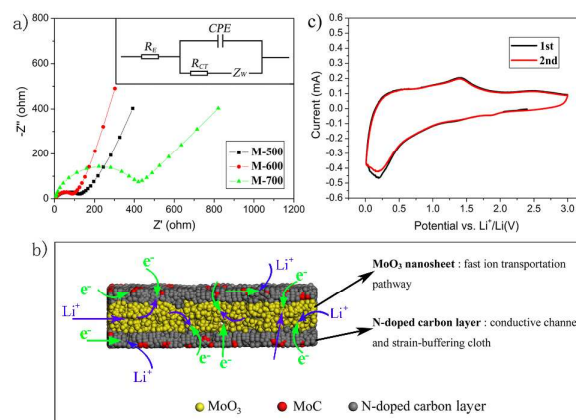
43
44 **Fig. 5** (a) Niquist plots of M-500, M-600 and M-700 over the
45 frequency range from 100 kHz to 0.01 Hz at the discharged
46 potential of 2.5 V after the 15th cycle. The inset is Equivalent
47 circuit for Niquist plots of M-500, M-600 and M-700. (b) A
48 representation shows the transportation paths for ion and
49 electron inside M-600. (c) Cyclic voltammogram curves of M-
50 600 in a half cell at a scanning rate of 0.5 mV s^{-1} ranged in 0.01-
51 3.0 vs Li/Li^+.
52
53
54 750 and 550 mAh g^{-1} at the current densities of 0.074 A g^{-1},
55 0.372 A g^{-1} and 0.744 A g^{-1}, respectively.[67] The capacities of
56 1110 mAh g^{-1} were achieved for pristine α-MoO_3 nanosheets
57 after 30 cycles at 0.074 A g^{-1}. It is clear that M-600 exhibits
58 better rate and cyclability performance than those values of
59 pristine MoO_3 nanosheets. Such good behavior can be
60 attributed to N-doped carbon coating, which can cause the
61 improved conductivity of active materials and increase the
62 structural stability of M-600 during cycling. In addition, the
63 electrochemical properties of M-600 was also compared with
64 that of pure carbon coated MoO_3 and various morphology
65 MoO_x electrodes. The results were listed in Table S2. The
66 comparison demonstrates that N-doped electrodes can provide
67 better electrochemical performance than that of non-doped
68 electrodes and the prepared N-doped carbon encapsulated
69 MoO_3 nanosheets have superior electrochemical properties to
70 that previously reported in literature.
71   In order to further compare the conductivity of M-500, M-
72 600 and M-700 electrodes, electrochemical impedance
73 spectroscopy (EIS) measured at the discharged potential of 2.5
74 V after the 15th cycle were carried out. As shown in Fig. 5a,
75 each Niquist plot consisted of two parts, a semicircle in the
76 high-medium frequency and a sloping line in the low frequency
77 regions. It can be clearly seen that the diameter of semicircle
78 for M-600 was much smaller than that of M-500 and M-700.
79 Previous studies[68-70] showed that better interphase electronic
80 contact could reduce the high-medium frequency impedance
81 semicircle. For practical values, Niquist plots were investigated
82 by using the equivalent circuit given in the inset. In equivalent
83 circuit, R_E is the ohmic resistance of cell components and
84 electrolyte. R_{CT} represents the Faradic charge-transfer
85 resistance. CPE stands for constant phase elements (involving
86 double layer capacitance of R_{CT}) and Warburg impedance Z_W

This journal is © The Royal Society of Chemistry 20xx

J. Mater. Chem. A, 2015, **00**, 1-3 | **5**

ARTICLE

reflects the solid state diffusion. The Warburg slope of M-600 was higher than those of M-500 and M-700, further indicating faster ion diffusion in M-600 electrode. By fitting the equivalent circuit, the charge transfer resistances of M-500, M-600 and M-700 were 122.7 Ω, 77.9 Ω and 405.8 Ω, respectively. This indicates that M-600 exhibits the lowest electrical contact resistance between the current-collector and active particles, which can lead to rapid electron transport during the electrochemical Li-ion insertion/extraction and thus results in a high rate capability and reversible capacity. EIS was also tested on pristine MoO_3 for comparison with M-600. The Niquist plots of both materials (Fig. S7) evidently showed that the special 2D nanosheet-type morphology of M-600 had better interphase conductive contact than bulk MoO_3 due to much thinner thickness along z direction (along the direction of thickness) and N-doped carbon nanocoating, which not only decreased charge diffusion distance and promoted electronic transportation. The major reasons that M-600 has better ionic and electronic conductivities than M-500 and M-700 are summarized. First, the graphitization degree of M-600 is higher than that of M-500, which is beneficial to the conductivity of carbon materials. Second, agglomeration of nanoparticle reduces the conductivities of M-700 electrodes. Third, the 2D nanosheet structure covered with a thin nitrogen-doped carbon layer and MoC in M-600 facilitates a quicker penetration of ion and electron into electrodes (see Fig. 5b). Due to such excellent properties of M-600, the cyclic voltammogram (CV) tests of M-600 electrodes were carried out to clarify the electrochemical information of MoO_3/NC nanosheets during Li^+ insertion/extraction. As shown in Fig. 5c, one negative peak around 0.24 V can be observed in the first discharge process, which arise from the lithiation of molybdenum oxide. During the delithiation process in the 1st cycle, a broad peak was observed around 1.38 V, which can be attributed to the extraction of Li-ion. In the 2nd cycle, the redox couple at around 0.24/1.38 V was reversible, which suggests highly reversible lithiation and delithiation of electrode reaction for M-600.

The remarkable electrochemical performance for M-600 can be attributed to the structural differences from other three materials. Firstly, M-600 has good structural stability and electronic conductivity, because it has 2D nanosheet structure and is covered with a thin nitrogen-doped carbon layer. However, microscale α-MoO_3 with bulk morphology can be readily subjected to structural pulverization caused by dramatic volume change, which results in poor cycling stability. Secondly, the graphitization degree of M-600 is higher than that of M-500, which is beneficial to the conductivity of carbon materials. Higher percentage of pyridinic-N can enhance the lithium storage activity, which leads to higher reversible capacity than M-500. Last, apart from lower percentage of pyridinic-N, the mass production of inactive MoC deteriorates electrochemical activity in M-700, thus resulting in lower reversible capacity than that of M-600.

Conclusions

MoO_3 nanosheets encapsulated with thin N-doped carbon layer have been synthesized via solid state thermolysis of layered MoO_3/dodecylamine composites at 600 ^{o}C under nitrogen atmosphere. The combined effect of 2D nanosheet-type structure and N-doped carbon encapsulation endows materials with high reversible capacity and is responsible for the superior rate performance with a capability of 490 mAh g^{-1} at 10 C and 370 mAh g^{-1} at 20 C. Due to the good structural flexibility and mechanical strength of N-doped carbon and MoC, the composites exhibit good cycle stability when used as the anode materials. After 60 cycles the anode still maintains a capacity of 1250 mAh g^{-1}. The results provide a new and facile route to the design of a composite with nitrogen-doped carbon for LIBs.
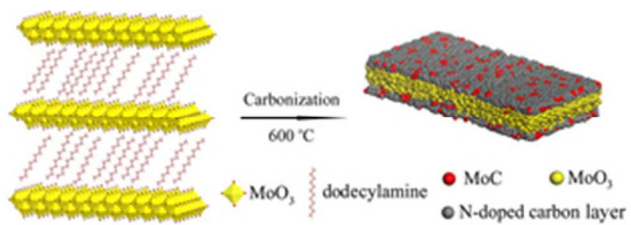
Acknowledgements

Notes and references

Y. Liu, H. Zhang, P. O, Z. Li, One-pot hydrothermal synthesized MoO_2 with high reversible capacity for anode application in lithium ion battery, Electrochim. Acta, 2013, **102**, 429.

K. Palanisamy, Y. Kim, H. Kim, J. M. Kim, W. Yoon, Self-assembled porous MoO_2/graphene microspheres towards high performance anodes for lithium ion batteries, J. Power Sources, 2015, **275**, 351.

X. Xue, Z. Chen, L. Xing, S. Yuan, Y. Chen, SnO_2/α-MoO_3 core-shell nanobelts and their extraordinarily high reversible capacity as lithium-ion battery anodes, Chem. Commun., 2011, **47,** 5205.

Z. Wang, S. Madhavi, X. W. Lou, Ultralong α-MoO_3 Nanobelts: Synthesis and Effect of Binder Choice on Their Lithium Storage Properties, J. Phys. Chem. C, 2012, **116**, 12508.

X. Li, J. Xu, L. Mei, Z. Zhang, C. Cui, H. Liu, J. Ma, S. Dou, Electrospinning of crystalline MoO_3@C nanofibers for high-rate lithium storage, J. Mater. Chem. A, 2015, **3**, 3257.

Y. S. Jung, S. Lee, D. Ahn, A. C. Dillon, S. Lee, Electrochemical reactivity of ball-milled MoO_{3-y} as anode materials for lithium-ion batteries, J. Power Sources, 2009, **188**, 286.

G. Zhao, N. Zhang, K. Sun, Electrochemical preparation of porous MoO_3 film with a high rate performance as anode for lithium ion batteries, J. Mater. Chem. A, 2013, **1**, 221.

B. K. Guo, X. P. Fang, B. Li, Y. F. Shi, C. Y. Ouyang, Y. S. Hu, Z. X. Wang, G. D. Stucky, L. Q. Chen, Synthesis and Lithium Storage Mechanism of Ultrafine MoO_2 Nanorods, Chem. Mater., 2012, **24**, 457.

S. H. Choi, Y. C. Kang, Crumpled Graphene-Molybdenum Oxide composite powders: preparation and application in lithium-ion batteries, ChemSusChem, 2014, **7**, 523.

H. J. Zhang, K. X. Wang, X. Y. Wu, Y. M. Jiang, Y. B. Zhai, C. Wang, X. Wei, J. S. Chen, MoO_2/Mo$_2$C heteronanotubes function as high-performance Li-ion battery electrode, Adv. Funct. Mater., 2014, **24**, 3399.

K. Sakaushi, J. Thomas, S. Kaskel, J. Eckert, Aqueous Solution Process for the Synthesis and Assembly of nanostructured one-dimensional α-MoO_3 electrode materials, Chem. Mater., 2013, **25**, 2557.

6 | *J. Mater. Chem. A*, 20xx, **00**, 1-3

This journal is © The Royal Society of Chemistry 20xx

1. P. Poizot, S. Laruelle, S. Grugeon, L. Dupont, J. M. Tarascon, Nano-sized transition-metal oxides as negative-electrode materials for lithium-ion batteries, Nature, 2000, **407**, 496.

2. J. Sun, H. Liu, X. Chen, D. G. Evans, W. Yang, X. Duan, Synthesis of graphene nanosheets with good control over the number of layers within the two-dimensional galleries of layered double hydroxides, Chem. Comm., 2012, **48**, 8126.

3. J. S. Chen, Y. L. Cheah, S. Madhavi, X. W. Lou, Fast synthesis of α-MoO_3 nanorods with controlled aspect ratios and their enhanced lithium storage capabilities, J. Phys. Chem. C, 2010, **114**, 8675.

4. Z. Wu, G. Zhou, L. Yin, W. Ren, F. Li, H. Cheng, Graphene/metal oxide composite electrode materials for energy storage, Nano Energy, 2012, **1**, 107.

5. Y. R. Wang, L. Zhang, Y. L. Wu, Y. J. Zhong, Y. Hu, X. W. Lou, Carbon-coated Fe_3O_4 microspheres with a porous multideck-cage structure for highly reversible lithium storage, Chem. Commun., 2015, **51**, 6921.

6. G. X. Gao, H. B. Wu, S. J. Ding, X. W. Lou, Preparation of carbon-coated $NiCo_2O_4@SnO_2$ hetero-nanostructures and their reversible lithium storage properties, Small, 2015, **11**, 432.

7. G. X. Gao, L. Yu, H. B. Wu, X. W. Lou, Hierarchical tubular structure constructed by carbon-coated α-Fe_2O_3 nanorods for highly reversible lithium storage, Small, 2014, **10**, 1741.

8. Z. Wang, Z. Wang, S. Madhavi, X. W. Lou, α -Fe_2O_3-mediated growth and carbon nanocoating of ultrafine SnO_2 nanorods as anode materials for Li-ion batteries, J. Mater. Chem., 2012, **22**, 2526.

9. X. W. Lou, C. M. Li, L. A. Archer, Designed Synthesis of Coaxial $SnO_2@carbon$ Hollow Nanospheres for Highly Reversible Lithium Storage, Adv. Mater., 2009, **21**, 2536.

10. Z. Wang, J. S. Chen, T. Zhu, S. Madhavi, X. W. Lou, One-pot synthesis of uniform carbon-coated MoO_2 nanospheres for high-rate reversible lithium storage, Chem. Commun., 2010, **46**, 6906.

11. Z. Wang, Z. Wang, W. Liu, W. Xiao, X. W. Lou, Amorphous $CoSnO_3@C$ nanoboxes with superior lithium storage capability, Energy Environ. Sci., 2013, **6**, 87.

12. Z. S. Wu, W. Ren, L. Wen, L. Gao, J. Zhao, Z. Chen, G. Zhou, F. Li, H. M. Cheng, Graphene anchored with Co_3O_4 nanoparticles as anode of lithium ion batteries with enhanced reversible capacity and cyclic performance, ACS Nano, 2010, **4**, 3187.

13. Z. S. Wu, D. W. Wang, W. Ren, J. Zhao, G. Zhou, F. Li, H. M. Cheng, Anchoring hydrous RuO_2 on graphene sheets for high-performance electrochemical capacitors, Adv. Funct. Mater., 2010, **20**, 3595.

14. X. Y. Yu, H. Hu, Y. W. Wang, H. Y. Chen, X. W. Lou, Ultrathin MoS_2 nanosheets supported on N-doped carbon nanoboxes with enhanced lithium storage and electrocatalytic properties, Angew. Chem. Int., Ed., 2015, **54**, 7395.

15. G. X. Gao, H. B. Wu, X. W. Lou, Citrate-assisted growth of $NiCo_2O_4$ nanosheets on reduced graphene oxides for highly reversible lithium storage, Adv. Energy Mater., 2014, **4**, 1400422.

16. J. S. Chen, Y. L. Tan, C. M. Li, Y. L. Cheah, D. Y. Luan, S. Madhavi, F. Y. C. Boey, L. A. Archer, X. W. Lou, Constructing hierarchical spheres from large ultrathin anatase TiO_2 nanosheets with nearly 100% exposed (001) facets for fast reversible lithium storage, J. Am. Chem. Soc., 2010, **132**, 6124.

17. Z. S. Wu, W. Ren, L. Xu, F. Li, H. M. Cheng, Doped graphene sheets as anode materials with superhigh rate and large capacity for lithium ion batteries, ACS Nano, 2011, **5**, 5463.

18. C. Wang, G. Shao, Z. Ma, S. Liu, W. Song, J. Song, Constructing $Fe_3O_4@N$-rich Carbon Core-Shell Microspheres as Anode for Lithium Ion Batteries with Enhanced Electrochemical Performance, Electrochim. Acta, 2014, **130**, 679.

19. Y. Fu, H. Ming, Q. Zhou, L. Jin, X. Li, J. Zheng, Nitrogen-doped carbon coating inside porous TiO_2 using small nitrogen-containing molecules for improving performance of lithium-ion batteries, Electrochim. Acta, 2014, **134**, 478.

20. M. Ara, V. R. Chitturi, S. O. Salley, K. Y. Simon Ng, Nitrogen-doped Carbon-coated Sn_xO_y (x = 1 and y = 0 and 2) Nanoparticles for Rechargeable Li-Ion Batteries, Electrochim. Acta, 2015, **161**, 269.

21. H. Ming, J. Ming, X. Li, Q. Zhou, H. Wang, L. Jin, Y. Fu, J. Adkins, J. Zheng, Hierarchical $Li_4Ti_5O_{12}$ particles co-modified with C&N towards enhanced performance in lithium-ion battery applications, Electrochim. Acta, 2014, **116**, 224.

22. H. Tao, M. Huang, L. Fan, X. Qu, Effect of nitrogen on the electrochemical performance of core-shell structured Si/C nanocomposites as anode materials for Li-ion batteries, Electrochim. Acta, 2013, **89**, 394.

23. Y. Fang, Y. Lv, R. Che, H. Wu, X. Zhang, D. Gu, G. Zheng, D. Y. Zhao, Two-Dimensional Mesoporous Carbon Nanosheets and Their Derived Graphene Nanosheets: Synthesis and Efficient Lithium Ion Storage, J. Am. Chem. Soc., 2013, **135**, 1524.

24. M. Zhao, Q. Zhang, J. Huang, F. Wei, Hierarchical Nanocomposites Derived from Nanocarbons and Layered Double Hydroxides-Properties, Synthesis, and Applications, Adv. Funct. Mater., 2012, **22**, 675.

25. G. Ning, C. Xu, Y. Cao, X. Zhu, Z. Jiang, Z. Fan, W. Qian, F. Wei, J. Gao, Chemical vapor deposition derived flexible graphene paper and its application as high performance anodes for lithium rechargeable batteries, J. Mater. Chem. A, 2013, **1**, 408.

26. H. Li, H. Zhou, Enhancing the performances of Li-ion batteries by carbon-coating: present and future, Chem. Commun., 2012, **48**, 1201.

27. Y. Jing, Q. Pan, Z. Cheng, X. Dong, Y. Xiang. Direct thermal intercalation of amine into layered MoO_3, Mater. Sci. Eng. B, 2007, **138**, 55.

28. W. X. Ji, R. Shen, R. Yang, G. Y. Yu, X. F. Guo, L. M. Peng, W. P. Ding, Partially nitrided molybdenum trioxide with promoted performance as an anode material for lithium-ion batteries, J. Mater. Chem. A, 2014, **2**, 699.

29. D. Zhou, H. P. Wu, Z. X. Wei, B. H. Han, Graphene-molybdenum oxynitride porous material with improved cyclic stability and rate capability for rechargeable lithium ion batteries, Phys. Chem. Chem. Phys., 2013, **15**, 16898.

30. X. Wang, R. Nesper, C. Villevieille, P. Novák, Ammonolyzed MoO_3 Nanobelts as Novel Cathode Material of Rechargeable Li-Ion Batteries, Adv. Energy Mater., 2013, **3**, 606.

31. J. Liu, S. Tang, Y. Lu, G. Cai, S. Liang, W. Wang, X. Chen, Synthesis of Mo_2N nanolayer coated MoO_2 hollow nanostructures as high-performance anode materials for lithium-ion batteries, Energy Environ. Sci., 2013, **6**, 2691.

32. B. Zhang, G. Cui, K. Zhang, P. Han, S. Dong, Molybdenum nitride/nitrogen-doped graphene hybrid material for lithium storage in lithium ion batteries, Electrochim. Acta, 2014, **150**, 15.

33. K. Zhang, L. Zhang, X. Chen, X. He, X. Wang, S. Dong, L. Gu, Z. Liu, C. Huang, G. Cui, Molybdenum Nitride/N-Doped Carbon Nanospheres for Lithium-O_2 Battery Cathode Electrocatalyst, ACS Appl. Mater. Interfaces, 2013, **5**, 3677.

34. Z. Li, Z. W. Xu, H. L. Wang, J. Ding, B. Zahiri, C. M. B. Holt, X. H. Tan, D. Mitlin, Colossal pseudocapacitance in a high functionality-high surface area carbon anode doubles the energy of an asymmetric, Energy. Environ. Sci., 2014, **7**, 1708.

35. L. G. Bulusheva,, A. V. Okotrub, A. G. Kurenya, H. Zhang, H. Zhang, X. Chen, H. Song, Electrochemical properties of nitrogen-doped carbon nanotube anode in Li-ion batteries, Carbon, 2011, **49**, 4013.

36. Y. Liu, T. Chen, T. Lu, Z. Sun, D. H. C. Chua, L. Pan, Nitrogen-doped porous carbon spheres for highly efficient capacitive deionization, Electrochim.Acta, 2015, **158**, 403.

This journal is © The Royal Society of Chemistry 20xx

J. Mater. Chem. A, 2015, **00**, 1-3 | **7**

1 T. V. Khai, H. G. Na, D. S. Kwak, Y. J. Kwon, H. Ham, K. B. Shim, H. W. Kim, Influence of N-doping on the structural and photoluminescence properties of graphene oxide films, Carbon, 2012, **50**, 3799.

2 X. Meng, H. Cui, J. Dong, J. Zheng, Y. Zhu, Z. Wang, J. Zhang, S. Jia, J. Zhao, Z. Zhu, Synthesis and electrocatalytic performance of nitrogen-doped macroporous carbons, J. Mater. Chem. A, 2013, **1**, 9469.

3 T. N. Huan, T. V. Khai, Y. Kang, K. B. Shim, H. Chung, Enhancement of quaternary nitrogen doping of graphene oxide via chemical reduction prior to thermal annealing and an investigation of its electrochemical properties, J. Mater. Chem., 2012, **22**, 14756.

4 C. Han, X. Bo, Y. Zhang, M. Li, L. Guo, One-pot synthesis of nitrogen and sulfur co-doped onion-like mesoporous carbon vesicle as an efficient metal-free catalyst for oxygen reduction reaction in alkaline solution, J. Power Sources, 2014, **272**, 267.

5 N. Gavrilov, I. A. Pasti, M. Vujkovic, J. T. Sejdic, G. C. Marjanovic, S. V. Mentus, High-performance charge storage by N-containing nanostructured carbon derived from polyaniline, Carbon, 2012, **50**, 3915.

6 H. Xiao, Z. G. Shao, G. Zhang, Y. Gao, W. Lu, B. L. Yi, Fe-N-carbon black for the oxygen reduction reaction in sulfuric acid, Carbon, 2013, **57**, 443.

7 P. Su, H. Xiao, J. Zhao, Y. Yao, Z. Shao, C. Li, Q. H. Yang, Nitrogen-doped carbon nanotubes derived from Zn‑Fe-ZIF nanospheres and their application as efficient oxygen reduction electrocatalysts with in situ generated iron species, Chem. Sci., 2013, **4**, 2941.

8 A. L. M. Reddy, A. Srivastava, S. R. Gowda, H. Gullapalli, M. Dubey, P. M. Ajayan, Synthesis of nitrogen-doped graphene films for lithium battery application, ACS Nano, 2010, **4**, 6337.

9 C. C. Ma, X. H. Shao, D. P. Cao, Nitrogen-doped graphene nanosheets as anode materials for lithium-ion batteries: a first-principles study, J. Mater. Chem., 2012, **22**, 8911.

10 Z. Li, Z. Xu, X. Tan, H. Wang, C. M. B. Holt, T. Stephenson, B. C. Olsen, D. Mitlin, Mesoporous nitrogen-rich carbons derived from protein for ultra-high capacity battery anodes and supercapacitors, Energy Environ. Sci., 2013, **6**, 871.

11 W Chen, L Qie, Y Shen, Y Sun, L Yuan, X Hu, W Zhang, Y Huang, Superior lithium storage performance in nanoscaled MnO promoted by N-doped carbon webs, Nano Energy, 2013, **2**, 412.

12 Y. J. Cho, H. S. Kim, H. Im, Y. Myung, G. B. Jung, C. W. Lee, J. Park, M. Park, J. Cho, H. S. Kang, Nitrogen-Doped Graphitic Layers Deposited on Silicon Nanowires for Efficient Lithium-Ion Battery Anodes, J. Phys. Chem. C, 2011, **115**, 9451.

13 L.G. Bulusheva, A.V. Okotrub, A.G. Kurenya, H. Zhang, H. Zhang, X. Chen, H. Song, Electrochemical properties of nitrogen-doped carbon nanotube anode in Li-ion batteries, Carbon, 2011, **49**, 4013.

14 C Wang, W Shen, H. M. Liu, Nitrogen-doped carbon coated $Li_3V_2(PO_4)_3$ derived from a facile in situ fabrication strategy with ultrahigh-rate stable performance for lithium-ion storage, New J. Chem., 2014, **38**, 430.

15 L Chen, Y Zhang, C Lin, W Yang, Y Meng, Y Guo, M Li, D Xiao, Hierarchically porous nitrogen-rich carbon derived from wheat straw as an ultra-high-rate anode for lithium ion batteries, J. Mater. Chem. A, 2014, **2**, 9684.

16 H. B. Wang, C. J. Zhang, Z. H. Liu, L. Wang, P. X. Han, H. X. Xu, K. J. Zhang, S. M. Dong, J. H. Yao, G. L. Cui, Nitrogen-doped graphene nanosheets with excellent lithium storage properties, J. Mater. Chem., 2011, **21**, 5430.

17 J. Schwan, S. Ulrich, V. Batori, H. Ehrhardt, Raman spectroscopy on amorphous carbon films, J. Appl. Phys., 1996, **80**, 440.

18 J. Robertson, Diamond-like amorphous carbon, Mater. Sci. Eng. R., 2002, **37**, 129.

19 A. C. Ferrari, J. Robertson, Interpretation of Raman spectra of disordered and amorphous carbon, Phys. Rev. B, 2000, **61**, 14095.

20 H. Zhang, L. Gao, Y. Gong, Exfoliated MoO_3 nanosheets for high-capacity lithium storage, Electrochem. Commun., 2015, **52**, 67.

21 J. Guo, A. Sun, X. Chen, C. Wang, A. Manivannan, Cyclability study of silicon-carbon composite anodes for lithium-ion batteries using electrochemical impedance spectroscopy, Electrochim. Acta, 2011, **56**, 3981.

22 M. Gaberscek, J. Moskon, B. Erjavec, R. Dominko, J. Jamnik, The importance of interphase contacts in Li ion electrodes: the meaning of the high-frequency impedance arc, Electrochem. Solid-State Lett., 2008, **11**, 170.

23 D. Dees, E. Gunen, D. Abraham, A. Jansen, J. Prakash, Alternating current impedance electrochemical modeling of lithium-ion positive electrodes, J. Electrochem. Soc., 2005, **152**, 1409.

8 | *J. Mater. Chem. A*, 20xx, **00**, 1-3

This journal is © The Royal Society of Chemistry 20xx

Schematic of the fabrication process of MoO3/NC nanosheets
26x9mm (300 x 300 DPI)